

---

# Integration of optic flow into the sky compass network in the brain of the desert locust

Frederick Zittrell<sup>1,2</sup>, Kathrin Pabst<sup>2,3</sup>, Elena Carlomagno<sup>1,°</sup>, Ronny Rosner<sup>1</sup>, Uta Pegel<sup>1</sup>, Dominik M. Endres<sup>2,3</sup> and Uwe Homberg<sup>1,2,\*</sup>

<sup>1</sup>*Department of Biology, Philipps-Universität Marburg, Marburg, Germany*

<sup>2</sup>*Center for Mind, Brain and Behavior (CMBB), Philipps-Universität Marburg and Justus Liebig Universität Gießen*

<sup>3</sup>*Department of Psychology, Philipps-Universität Marburg, Marburg, Germany*

Correspondence\*:

Uwe Homberg  
Philipps-Universität Marburg  
Karl-von-Frisch Straße 8  
35043 Marburg  
Germany  
homberg@staff.uni-marburg.de

° Present Address: Department of Psychiatry, Philipps-Universität Marburg, Marburg, Germany.

2 Words: (5496 excluding appendix) 6219 (including appendix), Figures: 9, Tables: 0

## 3 **ABSTRACT**

4 Flexible orientation through any environment requires a sense of current relative heading that  
5 is updated based on self-motion. Global external cues originating from the sky or the earth's  
6 magnetic field and local cues provide a reference frame for the sense of direction. Locally, optic  
7 flow may inform about turning maneuvers, travel speed and covered distance. The central complex  
8 in the insect brain is associated with orientation behavior and largely acts as a navigation center.  
9 Visual information from global celestial cues and local landmarks are integrated in the central  
10 complex to form an internal representation of current heading. However, it is largely unclear which  
11 neurons integrate optic flow in the central-complex network. We recorded intracellularly from  
12 neurons in the locust central complex while presenting lateral grating patterns that simulated  
13 translational and rotational motion to identify these sites of integration. Certain types of central-  
14 complex neurons were sensitive to visual self-motion independent of the type and direction of  
15 simulated motion. Columnar neurons innervating the noduli, paired central-complex substructures,  
16 were tuned to the direction of simulated horizontal turns. Modelling the connectivity of these  
17 neurons with a system of proposed compass neurons can account for rotation-direction specific  
18 shifts in the activity profile in the central complex corresponding to turn direction. Our model  
19 is similar but not identical to the mechanisms proposed for angular velocity integration in the  
20 navigation compass of the fly *Drosophila*.

21 **Keywords:** optic flow, sky compass, desert locust, orientation, computational model, central complex, head direction, intracellular  
22 recordings

## 1 INTRODUCTION

23 Animals navigate to feed, escape, migrate, and reproduce. Navigational tasks require a sense of current  
24 travel direction, which must be anchored to external cues and updated by internal cues, generated by  
25 ego-motion. Celestial cues are used as external cues by many insects, such as bees (von Frisch, 1946),  
26 ants (Fent, 1986), butterflies (Perez et al., 1997), dung beetles (Byrne et al., 2003), fruit flies (Weir and  
27 Dickinson, 2012), and caterpillars (Uemura et al., 2021). The sun and the skylight polarization pattern  
28 provide a reliable reference for dead reckoning (Gould, 1998). Internal cues, such as proprioceptive  
29 feedback (Wittlinger et al., 2006) and optic flow (Srinivasan, 2015; Stone et al., 2017), provide information  
30 about traveling speed and covered distance and may update the inner sense of direction in the absence of  
31 external cues. Only the flexible combination of information from external and internal cues enables robust  
32 and efficient navigation behavior, such as path integration (Heinze et al., 2018).

33 The central complex (CX), a midline spanning group of neuropils, houses the internal sense of direction  
34 in the brain of insects. It consists of the protocerebral bridge (PB), the lower (CBL) and upper (CBU)  
35 division of the central body, also termed ellipsoid- and fan-shaped body, and a pair of layered noduli (NO),  
36 and is associated with learning, memory and, importantly, spatial orientation (Pfeiffer and Homberg, 2014).  
37 The PB and the CBL are subdivided into series of 16 or 18 columns that are connected across the brain  
38 midline in a precise topographic manner (Pfeiffer and Homberg, 2014; Hulse et al., 2021; Hensgen et al.,  
39 2022).

40 CX neurons in various insect species are tuned to celestial cues (Heinze, 2017; Honkanen et al., 2019)  
41 and encode the solar azimuth in a compass-like manner in the locust (Pegel et al., 2019; Zittrell et al., 2020).  
42 Silencing compass neurons in the CX impairs navigation behavior in the fruit fly (Giraldo et al., 2018),  
43 showing the necessity of the CX for this behavior. Like mammalian head direction cells (Taube, 1998, 2007),  
44 specific CX neuron populations are tuned to the animal's current heading (Seelig and Jayaraman, 2015;  
45 Hulse and Jayaraman, 2020). This internal heading estimate is multimodally tethered to environmental cues,  
46 such as visual compass cues and wind direction (Okubo et al., 2020), but also operates without external  
47 input, because internal cues from self motion are likewise integrated (Green et al., 2017; Turner-Evans  
48 et al., 2017; Green and Maimon, 2018).

49 Although the understanding of the CX network has made considerable progress, mainly owing to research  
50 in the fruit fly, and plausible models explaining network computations for navigation have been proposed  
51 (Stone et al., 2017), it is largely unclear at which network stages optic flow input is integrated in the  
52 sky compass network. To investigate this, we recorded intracellularly from various CX neurons in the  
53 desert locust (*Schistocerca gregaria*), a long-distance migratory insect, while stimulating laterally with  
54 wide-field visual motion that simulated self-motion to the animal. We analyzed general motion sensitivity  
55 for translational and rotational self-motion directions and tested whether the neural responses to opposing  
56 motion directions were discriminated (direction selectivity).

57 We implemented an algorithmic model (in the sense of Marr and Poggio (1979)) of the CX circuit which  
58 integrates visual self-motion cues with head direction representation. Modeling was guided by data on two  
59 types of columnar neurons with one being sensitive to the direction of simulated horizontal turns.

## 2 METHODS

### 60 2.1 Animals and preparation

61 Desert locusts (*Schistocerca gregaria*) were kept and dissected as described previously (Zittrell et al.,  
62 2020). Animals were reared in large groups (gregarious state) at 28 °C with a 12 h / 12 h light / dark cycle;  
63 adult locusts from either sex were used for experiments. Limbs and wings were cut off, the animals were  
64 fixed on a metal holder with dental wax, and the head capsule was opened frontally, providing access to the  
65 brain. The esophagus was cut inside the head, close to the mandibles, and the abdomen's end was cut off to  
66 take out the whole gut through this opening. The brain was freed of fat, trachea and muscle tissue and was  
67 stabilized with a small metal platform that was fixed to the head capsule. Shortly before recording, the  
68 brain sheath was removed at the target site with forceps, permitting penetration with sharp glass electrodes.  
69 The brain was kept moist with locust saline (Clements and May, 1974) throughout the experiment.

### 70 2.2 Intracellular recording and histology

71 Sharp microelectrodes were drawn with a Flaming/Brown filament puller (P-97; Sutter Instrument), their  
72 tips filled with Neurobiotin tracer (Vector Laboratories; 4 % in 1 mol · l<sup>-1</sup> KCl) and their shanks filled  
73 with 1 mol · l<sup>-1</sup> KCl. Intracellular recordings were amplified with a custom-built amplifier and digitized  
74 with a 1401plus (Cambridge Electronic Device, CED) analog-digital converter (ADC) or amplified with a  
75 BA-01X (npi electronic GmbH) and digitized with a Micro mkII with an ADC12 expansion unit (CED).  
76 Signals were monitored with a custom-built audio monitor and recorded with Spike2 (CED). Neurons were  
77 traced by electrically injecting Neurobiotin (~1 nA positive current for several minutes). Each neuron  
78 presented in this study originates from a different specimen. Brains were dissected and immersed in fixative  
79 (4 % paraformaldehyde, 0.25 % glutaraldehyde and 0.2 % saturated picric acid, diluted in 0.1 mol · l<sup>-1</sup>  
80 phosphate buffered saline [PBS]) over night, followed by optional storage at 4°C in sodium phosphate  
81 buffer until further processing. Brains were rinsed in PBS (4 × 15 min) and incubated with Cy3-conjugated  
82 streptavidin (Dianova; 1:1,000 in PBS with 0.3 % Triton X-100 [PBT]) for 3 d at 4°C. After rinsing in  
83 PBT (2 × 30 min) and PBS (3 × 30 min), they were dehydrated in an ascending ethanol series (30 %, 50  
84 %, 70 %, 90 %, 95 %, and 2 × 100 %, 15 min each) and cleared in a 1:1 solution of ethanol (100 %) and  
85 methyl salicylate for 20 min and in pure methyl salicylate for 35 min, to finally mount them in Permount  
86 (Fisher Scientific) between two coverslips. For anatomical analysis, brains were scanned with a confocal  
87 laser-scanning microscope (Leica TCS SP5; Leica Microsystems). Cy3 fluorescence was elicited with a  
88 diode pumped solid-state laser at 561 nm wavelength. The resulting image stacks were processed with  
89 Amira 6.5 (ThermoFisher Scientific, Waltham, MA) and Affinity Photo (Serif, Nottingham, UK). The  
90 chirality of some neurons could not be determined because multiple neurons of the same neuron class but  
91 on both brain sides were stained in these cases.

### 92 2.3 Experimental Design

93 We used two monitors (FT10TMB, 10“, 1024x768 px at 60 Hz, Faytech, Shenzhen, China) that were  
94 placed 12.7 cm apart on the left and right side of the animal. They were mounted vertically to present  
95 sinusoidal grayscale grating patterns (Figure 1A). The displays were covered with diffuser sheets to  
96 eliminate light polarization inherent to LCD monitors. The patterns were drawn on the inner center-square  
97 (15.35 cm edge length) of the displays, covering 62.3° of the visual field on each side. The monitor  
98 brightness amounted to 1.12 · 10<sup>11</sup> photons cm<sup>-2</sup> · s<sup>-1</sup> when displaying a black area and 7.09 · 10<sup>13</sup> ·  
99 cm<sup>-2</sup> · s<sup>-1</sup> when displaying a white area. Monitor brightness was measured using a digital spectrometer  
100 (USB2000; Ocean Optics) placed at the position of the locust head.

101 The grating patterns were animated to simulate self-motion to the animal. We tested translational (forward  
102 and backward) motion, yaw rotation (left and right turning), lift (upward and downward), and roll (counter  
103 clockwise and clockwise). Throughout this study, these direction labels refer to simulated self-motion  
104 directions and not absolute motion of the displayed patterns. Thus, “forward motion” means that both  
105 monitors displayed a grating pattern with horizontal bands (perpendicular to the locust’s body axis, cf.  
106 Figure 1A) that continuously moved from top to bottom. For the sake of readability, we use “visual motion”  
107 for this wide-field visual motion stimulation, although this term includes diverse visual stimulation types,  
108 such as looming objects, small moving targets or full-panoramic optic flow, neither of which we presented  
109 to the animals.

110 Each motion direction was tested in a series of trials; each trial consisted of two phases, a motion phase  
111 and an immediately following stationary phase (Figure 1B,B’). All phases in the same recording lasted for  
112 five or six seconds. Each series consisted of two to five trials; each trial was immediately followed by the  
113 next one, unless it was the last of the series. Neurons typically responded strongly to the pattern display  
114 switch between series. Therefore, each series of a given motion direction was preceded by an adaptation  
115 phase which was discarded; this phase was a single stationary phase of the same pattern used during the  
116 upcoming series, immediately followed by the first motion phase of the series. If the same motion direction  
117 was tested in more than one series, all trials were treated as if they belonged to the same series. Not all  
118 neurons could be tested for all motion directions due to recording instability.

119 A separate PC running MATLAB (R2019, MathWorks) with the Psychophysics toolbox (Brainard, 1997)  
120 was used to generate the grating patterns (Figure 1A). The sine gratings had a spatial resolution of 0.005  
121 cycles  $\cdot$  px<sup>-1</sup> (one sine cycle spanned 200 px) and were shifted with 2 cycles  $\cdot$  s<sup>-1</sup> during the motion  
122 phases. This PC was USB-connected to an Arduino Uno (Arduino) via which TTL pulses were sent to  
123 the ADC, recorded at 500 Hz. These pulses indicated grating pattern animation and onset of stimulation  
124 phases. Two squares with 30 px edge length in the top left corner of each display were used to indicate  
125 the presented motion type by flashing them white: Each motion type was assigned a distinct number of  
126 flashes (20 ms duration) that were generated at the end of the adaptation phase of each series. Each square  
127 was covered by a photo diode that picked up the white flashes and whose signal was recorded by the  
128 ADC at 200 Hz. This allowed for encoding the motion type of each stimulation series in the data file. The  
129 generation of each rectangle flash was also recorded via the Arduino as a TTL rectangle pulse of the same  
130 duration, which allowed for measuring the precise timing of stimulus display by cross correlating diode  
131 signal and TTL signal.

## 132 2.4 Statistical Analysis

133 Spikes were detected by median filtering (500 ms window width) the voltage signal and applying a  
134 manually chosen threshold. Spikes and non-spikes (gaps) within 2 ms time bins were counted during the  
135 whole 5 s long interval of each trial of stimulation condition. We chose 2 ms time bins for this analysis  
136 because this is the approximate length of the refractory period of the neurons.

### 137 2.4.1 Motion Sensitivity

138 We define motion sensitivity as a neuron’s property to have different firing rates during motion and  
139 stationary phases. We analyzed motion sensitivity for each tested neuron and motion direction by comparing  
140 the neuron’s firing rate during the motion phase with that during the previous stationary phase. Firing  
141 probabilities were computed by integrating prior knowledge about compass neuron activity in general and  
142 the condition-specific data from each neuron via Bayesian inference. For each neuron  $n$ , we computed

143 a posterior over three different hypotheses: First, that the firing probability in 2 ms time bins during the  
 144 motion phase  $r_m$  is lower than the firing probability  $r_s$  during the stationary phase,  $H(r_m < r_s)$ , second,  
 145 that the firing probabilities are equal  $H(r_m == r_s)$ , or third, that  $r_m$  exceeds  $r_s$ ,  $H(r_m > r_s)$ . A high  
 146 posterior for the first or third hypothesis would indicate motion sensitivity, while a high posterior for the  
 147 second hypothesis would indicate that the neuron does not respond to the motion stimulation.

148 Using Bayes' rule, we computed the posterior distribution  $P(H|D)$  over the three hypotheses  
 149  $H \in \{H(r_m < r_s), H(r_m == r_s), H(r_m > r_s)\}$  given the experimental data  $D$ , assuming an uniform  
 150 hypothesis prior, a Bernoulli observation model and a joint Beta prior for the firing probabilities. This joint  
 151 prior was restricted by the firing probability constraints expressed in each hypothesis, e.g. for  $H(r_m < r_s)$ ,  
 152 the probability  $P(r_m \geq r_s) = 0$  etc. For details, see appendix 5.1.

153 To summarize the information embedded in this posterior and to simplify comparison across multiple  
 154 neurons, we computed a single motion sensitivity score (MSS) per neuron and motion direction (dir):

$$MSS_{dir} = \begin{cases} H(r_m > r_s) & : 1 \\ H(r_m == r_s) & : 0 \\ H(r_m < r_s) & : -1 \end{cases} \quad (1)$$

155 We weight this score with the corresponding hypothesis posterior probability and sum across all neurons  
 156 of one type. The maximal value for one firing probability hypothesis is therefore equal to the number of  
 157 neurons of a given type.

158 Further, we computed absolute motion sensitivity scores (AMSS) for four motion categories (cat),  
 159 each comprised of two opposing motion directions  $A$  and  $B$ : translational motion (forward or backward  
 160 direction), yaw rotation (left or right turning), lift (upward or downward), and roll (counterclockwise or  
 161 clockwise):

$$AMSS_{cat} = 1 - [P(H(r_{m,A} == r_{s,A})|D) * P(H(r_{m,B} == r_{s,B})|D)] \quad (2)$$

162 where  $r_{m,A}$  and  $r_{m,B}$  are firing probabilities during stimulation with opposing motion directions in the  
 163 respective motion category. In other words, this score will be close to one if at least one motion direction  
 164 of a category elicits a strong deviation from the stationary firing probability. We sum this score across all  
 165 neurons of a given type.

## 166 2.4.2 Direction Selectivity

167 We define direction selectivity as a neuron's property to respond contrarily to two opposing motion  
 168 directions  $A$  and  $B$ . We analyzed direction selectivity in the four motion categories outlined above:  
 169 translation, yaw rotation, lift, and roll. In the following, the hypothesis  $H(r_{m,A} \geq r_{s,A}) = H(r_{m,A} >$   
 170  $r_{s,A}) \vee H(r_{m,A} == r_{s,A})$  where  $\vee$  indicates a logical or, and  $\wedge$  is a logical and.

171 We compute a direction sensitivity score as

$$DSS_{cat} = \begin{cases} [H(r_{m,A} \geq r_{s,A}) \wedge H(r_{m,B} < r_{s,B})] \vee [H(r_{m,A} > r_{s,A}) \wedge H(r_{m,B} == r_{s,B})] & : 1 \\ [H(r_{m,A} < r_{s,A}) \wedge H(r_{m,B} \geq r_{s,B})] \vee [H(r_{m,A} == r_{s,A}) \wedge H(r_{m,B} > r_{s,B})] & : -1 \\ \text{otherwise} & : 0 \end{cases} \quad (3)$$

172 For example,  $DSS_{translation}$  is +1(-1) if the firing probability does not decrease during forward(backward)  
 173 motion and decreases during backward(forward) motion, or if it increases during forward(backward) motion  
 174 and does not change during backward (forward) motion. It is 0 if the firing probability changes in the same

175 direction for both motion directions. We weight this score with the corresponding hypothesis posterior  
 176 probability and sum across all neurons of one type. The maximal value for one firing probability hypothesis  
 177 is therefore equal to the number of neurons of a given type, similar to  $MSS_{dir}$ .

178 As an indicator for the total number of neurons with any direction sensitivity at all, we computed the  
 179 expected absolute direction sensitivity score (ADSS):

$$\begin{aligned} \langle ADSS_{cat} \rangle &= P(H(r_{m,A} > r_{s,A})|D) * P(H(r_{m,B} < r_{s,B})|D) \\ &+ P(H(r_{m,A} < r_{s,A})|D) * P(H(r_{m,B} > r_{s,B})|D) \end{aligned} \quad (4)$$

180 This score can take values between 0 and 1, with values close to zero indicating no direction selectivity  
 181 and values close to one indicating direction selectivity, disregarding which motion direction elicits greater  
 182 firing rates. We sum this score across all neurons of a given type.

183 The appendix 5.1 comprises a power analysis for the analyses of motion sensitivity and direction  
 184 selectivity outlined above, indicating which difference in the recorded firing rates is considered evidence  
 185 for the hypothesis that a neuron fires more in one of the two conditions.

## 186 2.5 Computational Model

187 All computations were performed with the Python programming language (version 3.10.8) and the  
 188 Pandas (version 1.5.1) and PyTorch (version 1.13.0) libraries. Plots were created with the Matplotlib library  
 189 (version 3.5.3).

190 Our model comprises CL1a and CL2 neurons, adopting the projection schemes proposed by Heinze and  
 191 Homberg (2008). We assume that, as shown for E-PG and P-EN neurons in the fly (Turner-Evans et al.,  
 192 2017), CL1a neurons provide synaptic inputs to CL2 neurons in the PB, which in turn provide synaptic  
 193 inputs to CL1a neurons in the CBL. We further assume a combination of excitation and inhibition within  
 194 the CL1a-CL2 connectivity instead of excitatory loops paired with global inhibition, as has been proposed  
 195 for *Drosophila* (Turner-Evans et al., 2017). The firing rate neurons and synaptic connections in our model  
 196 are linearized around their operating point, thus approximating their non-linear dynamics. We previously  
 197 implemented this circuit with CL1a neurons exciting the CL2 neurons and CL2 neurons inhibiting the CL1a  
 198 neurons (Pabst et al., 2022), referred to as Model A. In the present work we implemented an additional  
 199 version of the model, referred to as Model B, where this relation is reversed because both versions are  
 200 equally likely given the available data.

201 We represent the CL1a-CL2 connectivity with a matrix  $M$  -  $M_A$  and  $M_B$  for Model A and Model  
 202 B, respectively. The matrix features additional self-recurrent connections at all neurons to enable the  
 203 maintenance of a baseline activity. Weights are uniform for all excitatory and inhibitory connections,  
 204 0.5 and -0.5, respectively. The network's activity is characterized by deviations from a baseline firing  
 205 rate, represented by a vector  $x_t$  with components  $x_{t,1:16}$  and  $x_{t,17:32}$  covering the CL1a and CL2 neurons,  
 206 respectively. The network is recurrent and iterated across time steps such that the activity at the next time  
 207 step can be computed from the current activity:

$$x_{t+1} = Mx_t \quad (5)$$

### 208 2.5.1 Maintenance of a Stable Head Direction Encoding

209 In the framework outlined above, maintenance of the head direction representation or CL1a activity  
 210 pattern  $x_{1:16}$  translates to an equality of  $x_{t,1:16}$  at time point  $t$  and  $x_{t+1,1:16}$  at the following time point,  
 211  $t + 1$ :

$$x_{t,1:16} = x_{t+1,1:16} \quad (6)$$

212 According to Equation 5, this is given if  $Mx_t = x_t$ . We refer to such  $x_t$  as stable states. We defined CL1a  
 213 activity targets  $\hat{x}_t$  matching the tuning observed across the PB (Pegel et al., 2019; Zittrell et al., 2020) and  
 214 employed an optimization algorithm to find stable states containing these targets. For more details, see  
 215 Pabst et al. (2022).

### 216 2.5.2 Rotation-induced Shifts of Compass Activity

217 We have previously described a possible computational mechanism that would produce a phasic shift  
 218 from  $x_t$  to  $x_{t+1}$  with Model A (Pabst et al., 2022), representing the influence of rotational flow inputs on  
 219 the compass system, putatively conveyed by TN or TB7 neurons. In the present work we adjusted the  
 220 modulatory effect to allow for broad arborizations in the CBL, in addition to the PB, and optimized the  
 221 synaptic weights to produce compass bump shifts with Models A and B. Furthermore, we applied additional  
 222 constraints to both models for better alignment with physiological data: In Model A we found that purely  
 223 feed-forward input to the CL1a and/or CL2 neurons cannot account for the observed shift behavior (Pabst  
 224 et al., 2022). Instead, we found a modulatory mechanism that successfully shifts the compass bump. In our  
 225 previous study we relaxed the original connectivity matrix  $M_A$  to allow for arborizations into adjacent PB  
 226 columns and optimized the weights in this relaxed matrix  $M_{A_r}$  to achieve shifts to either direction, adding  
 227 inhibitory or excitatory connections in up to two further PB columns on each side of all existing synapses.  
 228 We constrained these shift-matrices  $M_{A_r,c}$  and  $M_{B_r,c}$  to better account for available physiological data:  
 229 For the neurons modeled here, no arborizations broader than one column were found in the PB, while  
 230 arborizations, in the CBL, especially in the upper layers, do in fact span three to five columns (Heinze and  
 231 Homberg, 2008). We refer to these models as ‘relaxed and constrained models’.

## 3 RESULTS

232 We surveyed CX neurons at different integration stages for sensitivity to visually simulated self-motion  
 233 (Figures 1,2). In total 62 morphologically identified neurons with arborizations in the CX were studied  
 234 (Figure 2). These included 4 tangential input neurons (TL) to the CBL comprising the subtypes TL2 and  
 235 TL3 (Figure 2A), 21 CL1a columnar neurons connecting the CBL to the PB, two CL2 columnar neurons  
 236 connecting the PB, CBL and NO, five TB1 tangential neurons of the PB, three CPU1, seven CPU2 and one  
 237 CPU5 neurons connecting distinct columns of the PB and CBU to the lateral complex (CPU1, CPU2) or a  
 238 nodulus (CPU5), one CP1 and two CP2 neurons connecting the PB to distinct areas of the lateral complex  
 239 (Figure 2B), eight PoU pontine neurons (Figure 2B), and various TU-type tangential neurons of the CBU  
 240 (Figure 2A). We found sensitivity to visual self-motion in some neural classes while others did not respond  
 241 to the stimulation.

### 242 3.1 Visual Self-motion Sensitivity and Direction selectivity in the Central Complex

243 Neurons in most of the examined morphological classes shown in Figures 2A-C were not sensitive  
 244 to the moving gratings. Some of the tested TL-, CL1a-, and CPU2 neurons, however, were sensitive to  
 245 grating patterns moving in at least one motion direction (motion sensitivity; Figures 3A,3B). Response

246 scores, indicating the sign of the firing rate change due to visual self-motion perception, were likewise  
247 inconsistently distributed within these neuron classes. Overall, within a given neuron class, individual  
248 neurons responded with excitation, inhibition or not at all to the same stimulus, independent of their  
249 brain side of origin (Figures 3A,3B). Two CL2 neurons, however, were not only motion sensitive but  
250 also responded differently to opposing motion directions (direction selectivity, Figures 3A,3B,4, and  
251 Supplementary Figure 2).

## 252 3.2 Yaw-rotation is processed by CL2 neurons

253 We recorded from two mirror-symmetric CL2 neurons. One neuron had smooth, presumably postsynaptic  
254 arborizations in the left NO and in column R4 of the right half of the PB, and beaded processes in layers  
255 1-3 of column L2 in the left half of the CBL (Figure 4B). The second CL2 neuron had ramifications in  
256 the right NO, column L4 in left half of the PB, and column R2 in the right half of the CBL (Figure 4D).  
257 Both neurons were directionally selective for visual motion that simulated yaw rotation, but with opposite  
258 polarity (Figures 4A,A',C,C' and Supplementary Figure 2). The CL2 neuron with arborizations in the right  
259 half of the PB and in the left NO (unit 801<sup>R</sup>, Supplementary Figures 1 and 2) responded to right turns  
260 with an increase and to left turns with a decrease in firing rate, compared to baseline. The neuron was also  
261 weakly inhibited by forward motion. The CL2 neuron arborizing in the left half of the PB and the right  
262 NO (unit 800<sup>L</sup> in Supplementary Figures 1 and 2) on the other hand responded to left turns with an  
263 increase and to right turns with a decrease in firing rate. Responses to translational motion stimuli were  
264 not tested. CL2 neurons are part of the internal compass system in the locust CX (Pegel et al., 2018) and  
265 likely homologous neurons in *Drosophila* (P-EN) apparently signal rotational self-motion, updating the  
266 internal heading representation when the animal turns. Our data support the idea that the locust internal  
267 compass signal is also shifted during turns via asymmetric excitation and inhibition of CL2 neurons (Figure  
268 5B'). The site of this interaction may either be the NO (via TN neurons) or the PB (via TB7 neurons).  
269 Both cell types are, like their equivalents in *Drosophila*, the GLNO neurons and the SpsP neurons (Hulse  
270 et al., 2021) morphologically suited to provide asymmetric input to the CL2 population. Like in *Drosophila*  
271 P-EN neurons, the projections of locust CL2 neurons in the CBL are shifted by one column relative to the  
272 projections of CL1 neurons (Figures 5A,5B). A notable difference between compass representation in the  
273 locust and the *Drosophila* compass system is that the E-PG population activity peak in the EB results in  
274 two activity peaks with a fixed offset along the PB, while available data in the locust suggest a single peak  
275 along the PB that results from azimuthal tuning to celestial cues ((Pegel et al., 2019; Zittrell et al., 2020)).  
276 If so, locust CL2 neurons might have inhibitory connections to CL1a neurons (Figure 5B). However, these  
277 connections and their polarity are hypothetical as there are no data on functional connectivity in the locust  
278 CX. Alternatively, the observed tuning could be a consequence of the projection and connectivity patterns  
279 of CL1a and CL2 neurons.

## 280 3.3 Computational Model

### 281 3.3.1 Maintenance of a Stable Head Direction Encoding

282 Model A and B maintain an initial CL1a activity pattern with an activity maximum or compass bump  
283 representing head direction relative to a global cue, such as the sun, when no yaw rotation is simulated.  
284 The CL2 population's activity is constrained by the polarity of synapses: We have previously shown that  
285 with CL1a neurons exciting CL2 neurons in the PB and CL2 neurons inhibiting CL1a neurons in the CBL  
286 in Model A, each CL2 neuron must have the same activity as the CL1a neuron associated with the same  
287 PB column to maintain a stable CL1a activity pattern (Pabst et al., 2022). In contrast, in Model B, where

288 CL1a neurons inhibit CL2 neurons and CL2 neurons excite CL1a neurons instead, the CL2 activity pattern  
289 across the PB must be the inverse of the CL1a pattern for CL1a activity maintenance.

### 290 3.3.2 Rotation-induced Shifts of Compass Activity

291 Feed-forward input to the CL1a/CL2 neurons can induce compass bump shifts neither in Model A nor in  
292 Model B. However, the weights in relaxed versions of the connectivity matrices  $M_{A_r}$  and  $M_{B_r}$  (Figures  
293 6B,B') could be optimized to induce compass bump shifts in both versions of the model. Optimizations  
294 for both Model A and Model B resulted in a connectivity with excitatory synapses from CL1a onto CL2  
295 neurons in the PB, a characteristic of Model A during compass bump maintenance (Figures 6B,B'). In the  
296 'relaxed and constrained models', we allowed the optimizer to broaden arborizations of CL2 neurons in the  
297 CBL to more than one column and reduced arborizations of CL1a neurons in the PB to single columns  
298 (Heinze and Homberg, 2008). Compared to the results obtained with the 'unconstrained relaxed models',  
299 optimization converged at a solution where the weights for self-recurrent connections had greater absolute  
300 values (Figures 6C,C'). Lastly, we enabled the addition of connections among CL2 neurons of the same  
301 hemisphere during the optimization process. Projection patterns suggest that all CL2 neurons of the same  
302 hemisphere branch in the lower unit of the contralateral NO, like P-EN neurons in *Drosophila* (Wolff  
303 et al., 2015) and the bumblebee (Sayre et al., 2021). Optimization converged at a solution with excitatory  
304 and inhibitory connections among CL2 neurons branching in the same nodulus. With these additional  
305 connections, synapses from CL2 onto CL1a neurons are weaker than in the other model versions (Figures  
306 6D,D').

## 4 DISCUSSION

307 We analyzed the sensitivity to visually simulated self-motion in different neuron classes in the locust CX  
308 network, from input-providing neurons (TL, TU neurons) to intermediate stage neurons (CL1a, CL2, POU,  
309 and TB1) and output neurons (CPU1, CPU2, CPU5, CP1, and CP2). Neurons in most of the investigated  
310 classes were not sensitive to visual self-motion. We hardly encountered consistent responses within the  
311 same neuron class, suggesting that single cells flexibly switch their cue sensitivity based on the internal state  
312 of the animal and environmental conditions. Exceptions were CL2 neurons, which mirror-symmetrically  
313 encoded yaw rotation direction, depending on the brain hemisphere in which they arborized, suggesting a  
314 role in keeping the internal compass system up to date during turning. A large fraction of cell types studied  
315 here (TL, CL1a, CL2, TB1, CPU1, CPU2, CP1, CP2) are elements of the sky compass system in the CX of  
316 the locust (Vitzthum et al., 2002; Heinze et al., 2009; Bockhorst and Homberg, 2015; Pegel et al., 2018;  
317 Zittrell et al., 2020). These neurons are sensitive to the azimuth of an unpolarized light spot (simulated sun)  
318 as well as to the polarization pattern above the animal (simulated sky) matching the position of the sun  
319 (Zittrell et al., 2020). The preference angles for solar azimuth in columnar neurons of the PB showed that  
320 solar azimuth is represented topographically across the columns of the PB as illustrated in Figure 5. The  
321 lack of responses to large-field motion stimuli in most of these neurons is in contrast to data from Rosner  
322 et al. (2019), who showed that a majority of sky compass neurons in the locust CX (types TL, CL1, TB1,  
323 CPU1, CPU2) were sensitive to progressive motion simulated through moving gratings. The reason for  
324 these different results most likely lies in different preparations of the animals. While in this study, legs  
325 and wings were removed, animals in the study of Rosner et al. (2019) had their legs attached and could  
326 perform walking motion on a slippery surface. Therefore, while the responses to sky compass signals may  
327 be affected only mildly, differences in behavioral context and internal state apparently play a major role  
328 for the sensitivity of sky compass neurons to visually simulated self-motion. Neurons of the CBU (PoU,  
329 TU, CPU5) that are not directly involved in sky compass signaling, were, likewise, unresponsive to visual

330 self-motion. This coincides with studies on *Drosophila* that found that responsiveness of neurons of the  
331 fan-shaped body (corresponding to the locust CBU) to motion stimuli highly depended on whether the  
332 animals were actively engaged in flight (Weir and Dickinson, 2015; Shiozaki et al., 2020). It is therefore  
333 likely, as for neurons of the sky compass system, that neurons at this integration stage are silent in locusts  
334 under the constrained conditions of our experiments. H $\Delta$ b neurons in *Drosophila* (corresponding to PoU  
335 neurons in the locust) integrate external and internal self-motion cues to transform egocentric directions into  
336 world-centric coordinates (Lu et al., 2022; Lyu et al., 2022). The lack of mechanosensory feedback under  
337 our experimental conditions likely explains why PoU neurons did not respond to purely visual self-motion  
338 cues. Under such conditions, PoU neurons, instead, strongly respond to looming objects (Rosner and  
339 Homberg, 2013), thus they might rather be involved in escape reactions when quiescence is signaled by  
340 the body. In general, physiological activity of locust CX neurons is considerably affected by active leg  
341 movement (Rosner et al., 2019). In our study, the legs were cut off, eliminating any proprioceptive sensory  
342 feedback.

343 In contrast to the lack of responsiveness in most cell types, two mirror-symmetric CL2 neurons showed  
344 robust responses to simulated yaw rotation with opposite directional preference. Inspired by the proposed  
345 role of P-EN neurons in *Drosophila* (corresponding to CL2 neurons in the locust) in updating and shifting  
346 the activity peak across the columns of the PB, we developed a computational model testing the likely  
347 function of CL2 neurons in the locust. The computational model of the CL1a-CL2 network resembles the  
348 recurrent loop connectivity between E-PG and P-EN neurons accounting for angular velocity integration in  
349 the *Drosophila* CX (Turner-Evans et al., 2017, 2020; Hulse et al., 2021). However, distinct differences exist,  
350 based on the 360° angular representation in the locust PB (Pegel et al., 2019; Zittrell et al., 2020) compared  
351 to the 2 × 360° representation of space in the *Drosophila* PB. While in *Drosophila* E-PG neurons form a  
352 360° representation of space in the ellipsoid body, two opposite 180° representations of space would be  
353 topographically intercalated in the CBL of the locust (Figure 5A). In *Drosophila* P-EN and E-PG neurons  
354 are connected by recurrent excitatory loops with additional global inhibition (Turner-Evans et al., 2017). In  
355 the locust, instead, both inhibitory and excitatory connections between CL1a and CL2 neurons are required.  
356 Our model assumes homogeneously inhibitory or excitatory synapses from one neuron population onto  
357 the other. We implemented two versions of the same model, differing only in the polarity of CL1a-CL2  
358 connections. Both versions proved suitable for compass state maintenance but required different activity  
359 patterns in the CL2 population. The version of the model with CL1a neurons inhibited by and exciting  
360 CL2 neurons requires the CL2 population activity to equal that of the CL1a population. The reversed  
361 version of this model in turn requires the CL2 population activity to be the inverse of the CL1a activity  
362 pattern. Physiological data revealing the relationship between the activities of these two populations would  
363 aid model evaluation and refinement. Close to equal E-PG and P-EN bump positions have been found in  
364 *Drosophila* moving at a low angular velocity, with an offset increasing with angular velocity (Turner-Evans  
365 et al., 2017). Neither of our versions could perform a shift of compass activity with a feed-forward input  
366 only, which might be due to the fact that our models do not include a closed loop from one end of the  
367 PB/CBL to the other. The inclusion of further neuron types might in fact close this gap and is the prospect  
368 of future work. CL1b-d neurons (Heinze and Homberg, 2008; Heinze et al., 2009) might, in addition,  
369 further stabilize the compass representation during standstill or forward motion. Franconville et al. (2018)  
370 reported that connections from E-PG onto P-EN neurons in the PB are mediated by  $\Delta$ 7 neurons. As TB1  
371 and TB2 neurons cross the midline of the locust PB, they are, in addition to contralateral processes observed  
372 in some CL1 neurons innervating the innermost columns of the PB (Sayre et al., 2021), candidates for  
373 mediating ring closure. An internal compass representation must adapt to a new heading direction when  
374 the animal turns. In the CX, this is likely accomplished by integrating rotation cues of different modalities.

375 Two entry sites into the CX network for information on rotational self-motion have been proposed so far,  
376 based on work in the fruit fly: i) The PB, where neurons may receive asymmetric input excited depending  
377 on turning direction, conveyed via IbSpsP neurons (TB7 neurons in the locust) (Hulse et al., 2021). These  
378 neurons connect specifically to P-EN neurons (CL2 neurons in the locust). ii) The NO, where GLNO  
379 neurons (TN neurons in the locust) that receive input in the lateral complex and innervating one NO might  
380 be excited/inhibited depending on turning direction. P-EN neurons convey these asymmetric inputs to  
381 E-PG neurons via synapses in the ellipsoid body, leading to a shift of the internal heading representation  
382 according to turning (Green et al., 2017; Turner-Evans et al., 2017). We explored possible mechanisms  
383 inducing the compass bump shift on an algorithmic level.

384 Instead of an additive input, different modulations of the network connectivity can produce a shift of the  
385 compass network activity pattern. We adjusted the previously published modulatory effect (Pabst et al.,  
386 2022) to feature broader arborizations in both the PB and the CBL and repeated optimization with Models A  
387 and B. Relaxed versions (with broader arborizations in the PB and CBL) of both models could be optimized  
388 to shift the compass signal in both directions. Optimization of Model B converged at the same solution as  
389 optimization of Model A, with excitatory synapses from CL1a onto CL2 neurons in the PB, suggesting that  
390 Model A can better explain the behavior of the compass network. To obtain a better fit to physiological data,  
391 we narrowed down the width of arborizations in the CBL to three columns and we limited the arborizations  
392 in the PB to single columns. Again, optimization of Model A and B was successful and converged at  
393 modulated matrices with excitation in the PB in both cases. We further explored the possibility of synapses  
394 among CL2 neurons of the same hemisphere, which could occur in the lower units of the two NO and  
395 appear to be also present in *Drosophila* (Hulse et al., 2021). This additional degree of freedom rendered  
396 synapses from CL2 onto CL1a neurons mostly redundant for shifts. In contrast to the shift-inducing matrix  
397 presented previously (Pabst et al., 2022), the shift-inducing connectivity matrices shown here render a  
398 closed, ring-like architecture in the sky compass network. The linear model and discrete motion steps  
399 employed here are still quite abstract representations of the neuronal and behavioral characteristics of the  
400 locust. So far, our model is not dynamic; it switches between stable states but does not make the dynamics  
401 underlying the transitions explicit. We aim to increase the model's biological plausibility by implementing  
402 velocity dependence in future work but expect the general principles of maintaining and updating the  
403 compass bump to hold independently of the level of analysis.

## CONFLICT OF INTEREST STATEMENT

404 The authors declare that the research was conducted in the absence of any commercial or financial  
405 relationships that could be construed as a potential conflict of interest.

## AUTHOR CONTRIBUTIONS

406 FZ, RR, and UH designed the experiments, FZ, EC, UP and RR performed the experiments. FZ wrote  
407 manuscript. KP and DME designed the computational model and statistical analysis. KP revised the  
408 manuscript, analyzed the data and implemented the computational model with DME. DME and UH  
409 conceived, designed, and directed research, and helped write the manuscript. All authors contributed to the  
410 article and approved the submitted version.

## FUNDING

411 This work was supported by Deutsche Forschungsgemeinschaft (HO 950/28-1 to U. H. and EN 1152/3-1 to  
412 D. M. E.), and the cluster project “The Adaptive Mind”, funded by the Excellence Program of the Hessian  
413 Ministry of Higher Education, Research, Science and the Arts.

## ACKNOWLEDGMENTS

414 We thank Stefanie Jahn for preparing Figure 4D and Martina Kern for maintaining locust cultures.

## DATA AVAILABILITY STATEMENT

415 The datasets analyzed and generated for this study along with the code written for analysis and modeling  
416 can be found in the data\_UMR repository (<http://dx.doi.org/10.17192/fdr/76>).

## REFERENCES

- 417 Bockhorst, T. and Homberg, U. (2015). Amplitude and dynamics of polarization-plane signaling in the  
418 central complex of the locust brain. *Journal of Neurophysiology* 113, 3291–3311. doi:10.1152/jn.00742.  
419 2014
- 420 Brainard, D. (1997). The psychophysics toolbox. *Spatial Vision* 10, 433–436. doi:10.1163/  
421 156856897X00357
- 422 Byrne, M., Dacke, M., Nordström, P., Scholtz, C., and Warrant, E. (2003). Visual cues used by ball-  
423 rolling dung beetles for orientation. *Journal of Comparative Physiology A* 189, 411–418. doi:10.1007/  
424 s00359-003-0415-1
- 425 Clements, A. and May, T. E. (1974). Studies on locust neuromuscular physiology in relation to glutamic  
426 acid. *Journal of Experimental Biology* 60, 673–705. doi:10.1242/jeb.60.3.673
- 427 Fent, K. (1986). Polarized skylight orientation in the desert ant *Cataglyphis*. *Journal of Comparative*  
428 *Physiology A* 158, 145–150. doi:10.1007/BF01338557
- 429 Franconville, R., Beron, C., and Jayaraman, V. (2018). Building a functional connectome of the *Drosophila*  
430 central complex. *Elife* 7. doi:10.7554/eLife.37017
- 431 Giraldo, Y. M., Leitch, K. J., Ros, I. G., Warren, T. L., Weir, P. T., and Dickinson, M. H. (2018). Sun  
432 navigation requires compass neurons in *Drosophila*. *Current Biology* 28, 2845–2852. doi:10.1016/j.cub.  
433 2018.07.002
- 434 Gould, J. L. (1998). Sensory bases of navigation. *Current Biology* 8, R731–R738. doi:10.1016/  
435 S0960-9822(98)70461-0
- 436 Green, J., Adachi, A., Shah, K. K., Hirokawa, J. D., Magani, P. S., and Maimon, G. (2017). A neural circuit  
437 architecture for angular integration in *Drosophila*. *Nature* 546, 101–106. doi:10.1038/nature22343
- 438 Green, J. and Maimon, G. (2018). Building a heading signal from anatomically defined neuron types in the  
439 *Drosophila* central complex. *Current Opinion in Neurobiology* 52, 156–164. doi:10.1016/j.conb.2018.  
440 06.010
- 441 Heinze, S. (2017). Unraveling the neural basis of insect navigation. *Current Opinion in Insect Science* 24,  
442 58–67. doi:10.1016/j.cois.2017.09.001
- 443 Heinze, S., Gotthardt, S., and Homberg, U. (2009). Transformation of polarized light information in the  
444 central complex of the locust. *Journal of Neuroscience* 29, 11783–11793. doi:10.1523/JNEUROSCI.  
445 1870-09.2009

- 446 Heinze, S. and Homberg, U. (2008). Neuroarchitecture of the central complex of the desert locust: intrinsic  
447 and columnar neurons. *Journal of Comparative Neurology* 511, 454–478. doi:10.1002/cne.24796
- 448 Heinze, S., Narendra, A., and Cheung, A. (2018). Principles of insect path integration. *Current Biology* 28,  
449 1043–1058. doi:10.1016/j.cub.2018.04.058
- 450 Hensgen, R., Dippel, S., Hümmert, S., Jahn, S., Seyfarth, J., and Homberg, U. (2022). Myoinhibitory  
451 peptides in the central complex of the locust *Schistocerca gregaria* and colocalization with  
452 locustatachykinin-related peptides. *Journal of Comparative Neurology* 530, 2782–2801. doi:10.  
453 1002/cne.25374
- 454 Honkanen, A., Adden, A., da Silva Freitas, J., and Heinze, S. (2019). The insect central complex  
455 and the neural basis of navigational strategies. *Journal of Experimental Biology* 222, jeb188854.  
456 doi:10.1242/jeb.188854
- 457 Hulse, B. K., Haberkern, H., Franconville, R., Turner-Evans, D. B., Takemura, S.-Y., Wolff, T., et al. (2021).  
458 A connectome of the *Drosophila* central complex reveals network motifs suitable for flexible navigation  
459 and context-dependent action selection. *Elife* 10, e66039. doi:10.1101/2020.12.08.413955v3
- 460 Hulse, B. K. and Jayaraman, V. (2020). Mechanisms underlying the neural computation of head direction.  
461 *Annual Review of Neuroscience* 43, 31–54. doi:10.1146/annurev-neuro-072116-031516
- 462 Kass, R. E. and Raftery, A. E. (1995). Bayes factors. *Journal of the American Statistical Association* 90,  
463 773–795. doi:10.2307/2291091
- 464 Lu, J., Behbahani, A. H., Hamburg, L., Westeinde, E. A., Dawson, P. M., Lyu, C., et al. (2022).  
465 Transforming representations of movement from body- to world-centric space. *Nature* 601, 98–104.  
466 doi:10.1038/s41586-021-04191-x
- 467 Lyu, C., Abbott, L., and Maimon, G. (2022). Building an allocentric travelling direction signal via vector  
468 computation. *Nature* 601, 92–97. doi:10.1038/s41586-021-04067-0
- 469 Marr, D. and Poggio, T. (1979). A computational theory of human stereo vision. *Proceedings of the Royal*  
470 *Society of London. Series B. Biological Sciences* 204, 301–328. doi:10.1098/rspb.1979.0029
- 471 Okubo, T. S., Patella, P., D’Alessandro, I., and Wilson, R. I. (2020). A neural network for wind-guided  
472 compass navigation. *Neuron* 107, 924–940. doi:10.1016/j.neuron.2020.06.022
- 473 Pabst, K., Zittrell, F., Homberg, U., and Endres, D. M. (2022). A model for optic flow integration in  
474 locust central-complex neurons tuned to head direction. In *Proceedings of the Annual Meeting of*  
475 *the Cognitive Science Society*. vol. 44. Online available at: [https://escholarship.org/uc/  
476 item/17k48481](https://escholarship.org/uc/item/17k48481)
- 477 Pegel, U., Pfeiffer, K., and Homberg, U. (2018). Integration of celestial compass cues in the central  
478 complex of the locust brain. *Journal of Experimental Biology* 221, jeb171207. doi:10.1242/jeb.171207
- 479 Pegel, U., Pfeiffer, K., Zittrell, F., Scholtyssek, C., and Homberg, U. (2019). Two compasses in the  
480 central complex of the locust brain. *Journal of Neuroscience* 39, 3070–3080. doi:10.1523/JNEUROSCI.  
481 0940-18.2019
- 482 Perez, S. M., Taylor, O. R., and Jander, R. (1997). A sun compass in monarch butterflies. *Nature* 387,  
483 29–29. doi:10.1038/387029a0
- 484 Pfeiffer, K. and Homberg, U. (2014). Organization and functional roles of the central complex in the insect  
485 brain. *Annual Review of Entomology* 59, 165–184. doi:10.1146/annurev-ento-011613-162031
- 486 Rosner, R. and Homberg, U. (2013). Widespread sensitivity to looming stimuli and small moving objects  
487 in the central complex of an insect brain. *Journal of Neuroscience* 33, 8122–8133. doi:10.1523/  
488 JNEUROSCI.5390-12.2013
- 489 Rosner, R., Pegel, U., and Homberg, U. (2019). Responses of compass neurons in the locust brain to visual  
490 motion and leg motor activity. *Journal of Experimental Biology* 222, jeb196261. doi:10.1242/jeb.196261

- 491 Sayre, M. E., Templin, R., Chavez, J., Kempnaers, J., and Heinze, S. (2021). A projectome of the  
492 bumblebee central complex. *Elife* 10, e68911. doi:10.7554/eLife.68911
- 493 Seelig, J. D. and Jayaraman, V. (2015). Neural dynamics for landmark orientation and angular path  
494 integration. *Nature* 521, 186–191. doi:10.1038/nature14446
- 495 Shiozaki, H. M., Ohta, K., and Kazama, H. (2020). A multi-regional network encoding heading and  
496 steering maneuvers in *Drosophila*. *Neuron* 106, 126–141. doi:10.1016/j.neuron.2020.01.009
- 497 Srinivasan, M. V. (2015). Where paths meet and cross: navigation by path integration in the desert ant and  
498 the honeybee. *Journal of Comparative Physiology A* 201, 533–546. doi:10.1007/s00359-015-1000-0
- 499 Stone, T., Webb, B., Adden, A., Weddig, N. B., Honkanen, A., Templin, R., et al. (2017). An anatomically  
500 constrained model for path integration in the bee brain. *Current Biology* 27, 3069–3085. doi:10.1016/j.  
501 cub.2017.08.052
- 502 Taube, J. S. (1998). Head direction cells and the neurophysiological basis for a sense of direction. *Progress*  
503 *in Neurobiology* 55, 225–256. doi:10.1016/S0301-0082(98)00004-5
- 504 Taube, J. S. (2007). The head direction signal: origins and sensory-motor integration. *Annual Review of*  
505 *Neuroscience* 30, 181–207. doi:10.1146/annurev.neuro.29.051605.112854
- 506 Turner-Evans, D., Wegener, S., Rouault, H., Franconville, R., Wolff, T., Seelig, J. D., et al. (2017). Angular  
507 velocity integration in a fly heading circuit. *Elife* 6, e23496. doi:10.7554/eLife.23496.001
- 508 Turner-Evans, D. B., Jensen, K. T., Ali, S., Paterson, T., Sheridan, A., Ray, R. P., et al. (2020). The  
509 neuroanatomical ultrastructure and function of a biological ring attractor. *Neuron* 108, 145–163.  
510 doi:10.1016/j.neuron.2020.08.006
- 511 Uemura, M., Meglič, A., Zalucki, M. P., Battisti, A., and Belušič, G. (2021). Spatial orientation of social  
512 caterpillars is influenced by polarized light. *Biology Letters* 17, 20200736. doi:10.1098/rsbl.2020.0736
- 513 Vitzthum, H., Müller, M., and Homberg, U. (2002). Neurons of the central complex of the locust  
514 *Schistocerca gregaria* are sensitive to polarized light. *Journal of Neuroscience* 22, 1114–1125. doi:10.  
515 1523/JNEUROSCI.22-03-01114.2002
- 516 von Frisch, K. (1946). Die Tänze der Bienen. *Österreichische Zoologische Zeitschrift* 1, 1–48
- 517 von Hadeln, J., Hensgen, R., Bockhorst, T., Rosner, R., Heidasch, R., Pegel, U., et al. (2020).  
518 Neuroarchitecture of the central complex of the desert locust: tangential neurons. *Journal of Comparative*  
519 *Neurology* 528, 906–934. doi:10.1002/cne.24796
- 520 Weir, P. T. and Dickinson, M. H. (2012). Flying *Drosophila* orient to sky polarization. *Current Biology* 22,  
521 21–27. doi:10.1016/j.cub.2011.11.026
- 522 Weir, P. T. and Dickinson, M. H. (2015). Functional divisions for visual processing in the central brain of  
523 flying *Drosophila*. *Proceedings of the National Academy of Sciences of the United States of America*  
524 112, E5523–E5532. doi:10.1073/pnas.1514415112
- 525 Wittlinger, M., Wehner, R., and Wolf, H. (2006). The ant odometer: stepping on stilts and stumps. *science*  
526 312, 1965–1967. doi:10.1126/science.1128659
- 527 Wolff, T., Iyer, N. A., and Rubin, G. M. (2015). Neuroarchitecture and neuroanatomy of the *Drosophila*  
528 central complex: A gal4-based dissection of protocerebral bridge neurons and circuits. *Journal of*  
529 *Comparative Neurology* 523, 997–1037. doi:10.1002/cne.23705
- 530 Zittrell, F., Pfeiffer, K., and Homberg, U. (2020). Matched-filter coding of sky polarization results in an  
531 internal sun compass in the brain of the desert locust. *Proceedings of the National Academy of Sciences*  
532 *of the United States of America* 117, 25810–25817. doi:10.1073/pnas.2005192117

## 5 APPENDIX

### 5.1 Statistical Model and Power Analysis of Motion Sensitivity

We designed a Bayesian model for the evaluation of the experimental spiking data, to test the hypotheses that the firing probability of a motion phase  $r_m$  is smaller, equal or larger than the firing probability  $r_s$  during a stationary phase. We denote these hypotheses by  $H \in \{H(r_m < r_s), H(r_m == r_s), H(r_m > r_s)\}$ . Given the firing probabilities, we assume that the data  $D = (s_m, g_m, s_s, g_s)$  of one experiment, comprised of spikes  $s_m, s_s$  during motion/stationary phases and corresponding non-spikes/gaps  $g_m, g_s$ , are generated by a Bernoulli process with a refractory period of 2 ms, which is typical for the neurons we investigate. There might be additional dependencies between spikes that are not captured by a refractory Bernoulli process, but these are not relevant for our hypotheses. The Bernoulli observation probability is given by

$$P(D|r_m, r_s) = r_m^{s_m} (1 - r_m)^{g_m} \cdot r_s^{s_s} (1 - r_s)^{g_s} \quad (7)$$

Since we are interested in hypotheses about firing probabilities relationships, we define a joint symmetric Beta prior with parameters  $\alpha, \beta$  on  $r_m$  and  $r_s$ , constrained by the hypothesis we wish to evaluate. We choose a symmetric prior to avoid a-priori biases beyond  $H$ . For  $H(r_m < r_s)$ , this prior is

$$P(r_m, r_s|\alpha, \beta, H(r_m < r_s)) \propto B(r_m|\alpha, \beta)B(r_s|\alpha, \beta)\mathbb{I}(r_m < r_s) \quad (8)$$

where  $B(r_m|\alpha, \beta)$  is a Beta density in  $r_m$  and  $\mathbb{I}(r_m < r_s)$  is an indicator function which is 1 if the condition in the parentheses is true, and 0 otherwise. This indicator function ensures that only hypothesis-conforming  $r_m, r_s$  pairs have nonzero probability. The constant of proportionality can be obtained from the requirement that the prior be normalized. Thus, this prior can be written as

$$P(r_m, r_s|\alpha, \beta, H(r_m < r_s)) = \frac{2}{B(\alpha, \beta)^2} r_m^{\alpha-1} (1 - r_m)^{\beta-1} r_s^{\alpha-1} (1 - r_s)^{\beta-1} \mathbb{I}(r_m < r_s) \quad (9)$$

The prior resulting from  $H(r_m > r_s)$  can be obtained by inversion of the  $<$  in the indicator function, whereas the prior for  $H(r_m == r_s)$  is simply one Beta prior for both (equal) firing probabilities.

Since we are largely ignorant about the values of  $\alpha$  and  $\beta$ , we chose these parameters by maximizing the differential entropy subject to the condition that the average firing probability is  $\approx 0.05$  in a 2 ms time bin, which is typical for our neurons. We found  $\alpha = 0.96$  and  $\beta = 18.28$ , and used these values for the rest of the analysis.

To compute the hypothesis posterior

$$P(H|D) = \frac{P(D|H)P(H)}{\sum_H P(D|H)P(H)} \quad (10)$$

via Bayes' rule, we chose a uniform hypothesis prior  $P(H) = \frac{1}{3}$ . We evaluated the probability  $P(D|H)$  by marginalizing the firing probabilities using Equation 7 and Equation 9. For example, letting  $H = H(r_m < r_s)$ :

$$\begin{aligned}
P(D|H(r_m < r_s)) &= \int_0^1 dr_s \int_0^1 dr_m P(D, r_m, r_s | H(r_m < r_s)) \\
&= \int_0^1 dr_s \int_0^1 dr_m P(D|r_m, r_s) P(r_m, r_s | H(r_m < r_s)) \\
&= \frac{2}{B(\alpha, \beta)^2} \int_0^1 dr_s \int_0^1 dr_m r_m^{\alpha+s_m-1} (1-r_m)^{\beta+g_m-1} r_s^{\alpha+s_s-1} (1-r_s)^{\beta+g_s-1} \mathbb{I}(r_m < r_s) \\
&= \frac{2}{B(\alpha, \beta)^2} \int_0^1 dr_s \int_0^{r_s} dr_m r_m^{\alpha+s_m-1} (1-r_m)^{\beta+g_m-1} r_s^{\alpha+s_s-1} (1-r_s)^{\beta+g_s-1} \\
&= \frac{2B(\alpha + s_m, \beta + g_m)}{B(\alpha, \beta)^2} \int_0^1 dr_s r_s^{\alpha+s_s-1} (1-r_s)^{\beta+g_s-1} I_B(r_s, \alpha + s_m, \beta + g_m) \quad (11)
\end{aligned}$$

559 where  $I_B(r, \alpha, \beta)$  is an incomplete beta function in  $r$  with parameters  $\alpha, \beta$ . We solved the last integral by  
560 Taylor-expanding  $I_B(r_s, \alpha + s_m, \beta + g_m)$  to second order at  $\frac{\alpha+s_s}{\alpha+s_s+\beta+g_s}$ , which yields a good approximation  
561 as long as  $s_m \approx s_s$  and  $g_m \approx g_s$ . This is the case in our data.

562 The probability  $P(D|H(r_m > r_s))$  can be evaluated by simply switching the roles of  $r_m$  and  $r_s$  in  
563 the above derivation. For  $P(D|H(r_m == r_s))$ , where there is only one rate, the integrals can be solved  
564 analytically to yield the well-known result

$$P(D|H(r_m == r_s)) = \frac{B(\alpha + s_m + s_s, \beta + g_m + g_s)}{B(\alpha, \beta)}. \quad (12)$$

565 To facilitate interpretation of the values of the absolute motion sensitivity (AMSS, Equation 2) and the  
566 motion hypothesis posterior, which we use to average the motion sensitivity scores (MSS, Equation 1),  
567 we conducted a power analysis. We simulated 10,000 repetitions of a typical experiment in our study,  
568 where an animal is stimulated for 5 s with either stationary or motion input. We generated spikes according  
569 to the Bernoulli process assumption (Equation 7) with 2 ms time bins by drawing spike counts from a  
570 binomial distribution. The firing rate of the stationary phase was set to 25 Hz, which corresponds to a firing  
571 probability  $r_s = 0.05$  and  $N = 2500$  Bernoulli trials during a single run of the experiment. An experiment  
572 consisted of five simulated runs in the simulation. The firing probability during the motion phase was  
573 assumed to be a multiple of  $r_s$  in the range 1.15 . . . 1.30. This range is covered by a strongly responding  
574 neuron, see e.g. Figure 4A, right panel. To relate our motion sensitivity scores to standard measures used in  
575 statistical contexts, we evaluated the Bayes factor in favor of a changed firing rate during motion:

$$BF(r_m \neq r_s) = \frac{P(D|H(r_m > r_s)) + P(D|H(r_m < r_s))}{P(D|H(r_m == r_s))} \quad (13)$$

576 The simulation results are shown in Figure 7. The top panel shows the AMSS, the middle panel the  
577 corresponding Bayes factors. The dotted lines show the boundaries for weak and strong evidence according  
578 to Kass and Raftery (1995). For strong evidence, the firing rate ratio has to be greater than 1.25, which  
579 implies an average AMSS  $> 0.65$ . In the bottom panel, we plotted the hypothesis posterior, which we use  
580 for averaging of the MSS. Strong evidence for an increased firing rate (MSS=+1 in Figure 3A) requires  
581 MSS  $> 0.65$ .

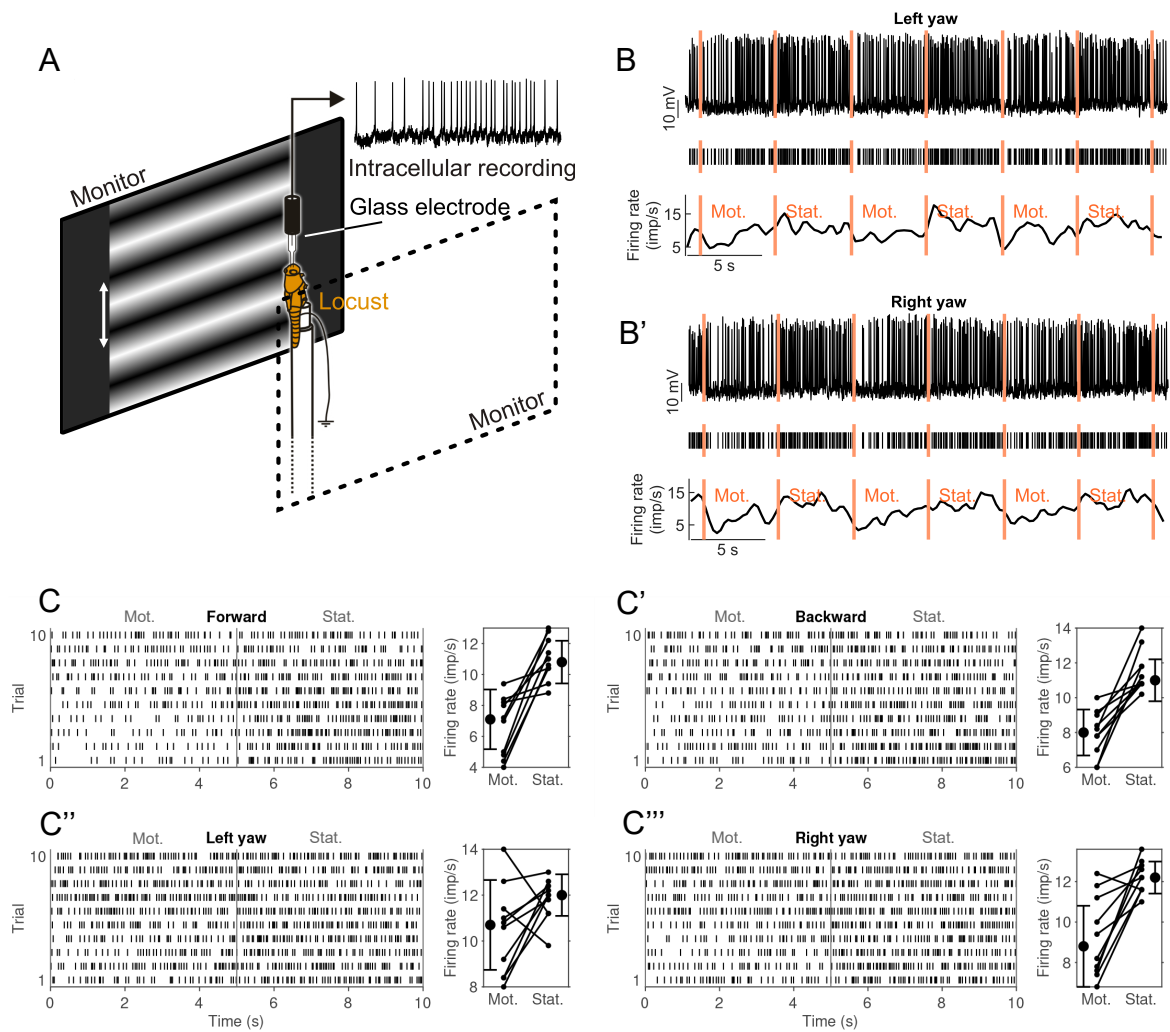


**Figure 1.** Experimental setup and visual-motion response of a CL1a neuron (neuron 550<sup>L</sup> in Supplementary Figures 1 and 2). (A) Animals were mounted vertically and stimulated with motion of sinusoidal grating patterns on two laterally placed monitors. (B) Response of a CL1a neuron to wide-field visual motion that simulated horizontal left turning (left yaw). Raw data (top), detected spikes (middle) and smoothed firing rate estimate (bottom). Vertical lines indicate onset of stimulation phases: Motion (Mot.) and stationary phase (Stat.) were alternated, each pair constituting one stimulation trial. (B') Same as B but for simulation of horizontal right turn motion (right yaw). (C) Raster plot (left) of all left-turn trials. Vertical line at 5 s indicates onset of stationary phase. Diagram on the right shows differences in firing rate between the motion (Mot) and stationary phase (Stat.) for each trial and mean firing rates for all trials. Error bars denote standard deviation. (C', C'', C''') Same as C but for (C') backward motion, (C'') left yaw and (C''') right yaw rotation.

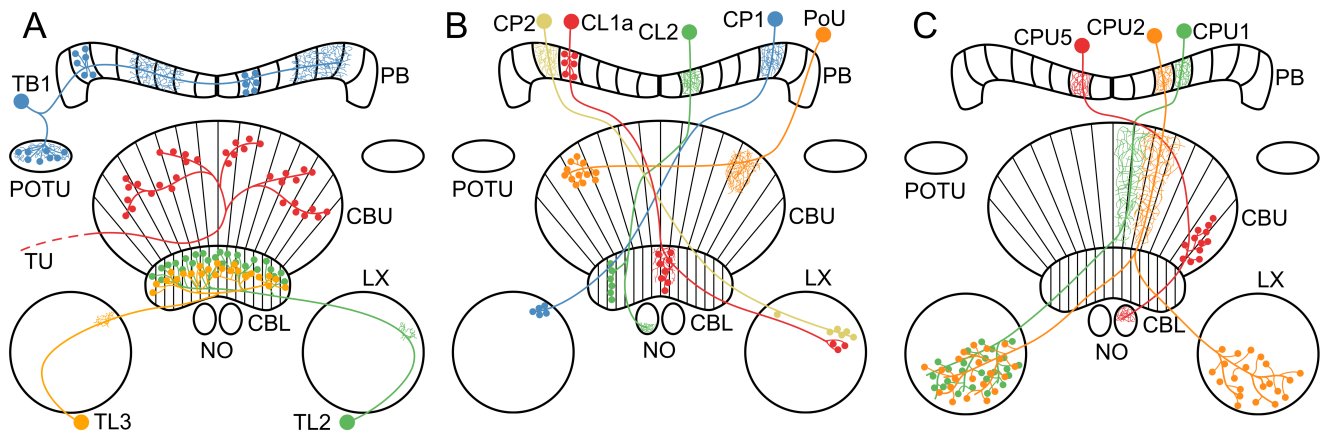


**Figure 2.** Morphology of neuron classes analyzed in this study. **(A–C)** Schematics of the locust central complex and associated neuropils (CBL, lower division of the central body; CBU, upper division of the central body; LX, lateral complex; NO, noduli; PB, protocerebral bridge; POTU, posterior optic tubercle) with individual neurons from different classes superimposed. Large dots indicate somata, small dots indicate axonal (presynaptic) arborizations, and fine lines indicate dendritic (postsynaptic) arborizations. **(A)** Tangential neurons. We classified TU neurons as a group of diverse neurons that only have in common that they have large presynaptic arborizations in the CBU and input regions outside the central complex. Wiring schematics based on (von Hadeln et al., 2020). **(B,C)** Columnar neurons. Wiring schematics based on (Heinze and Homberg, 2008).

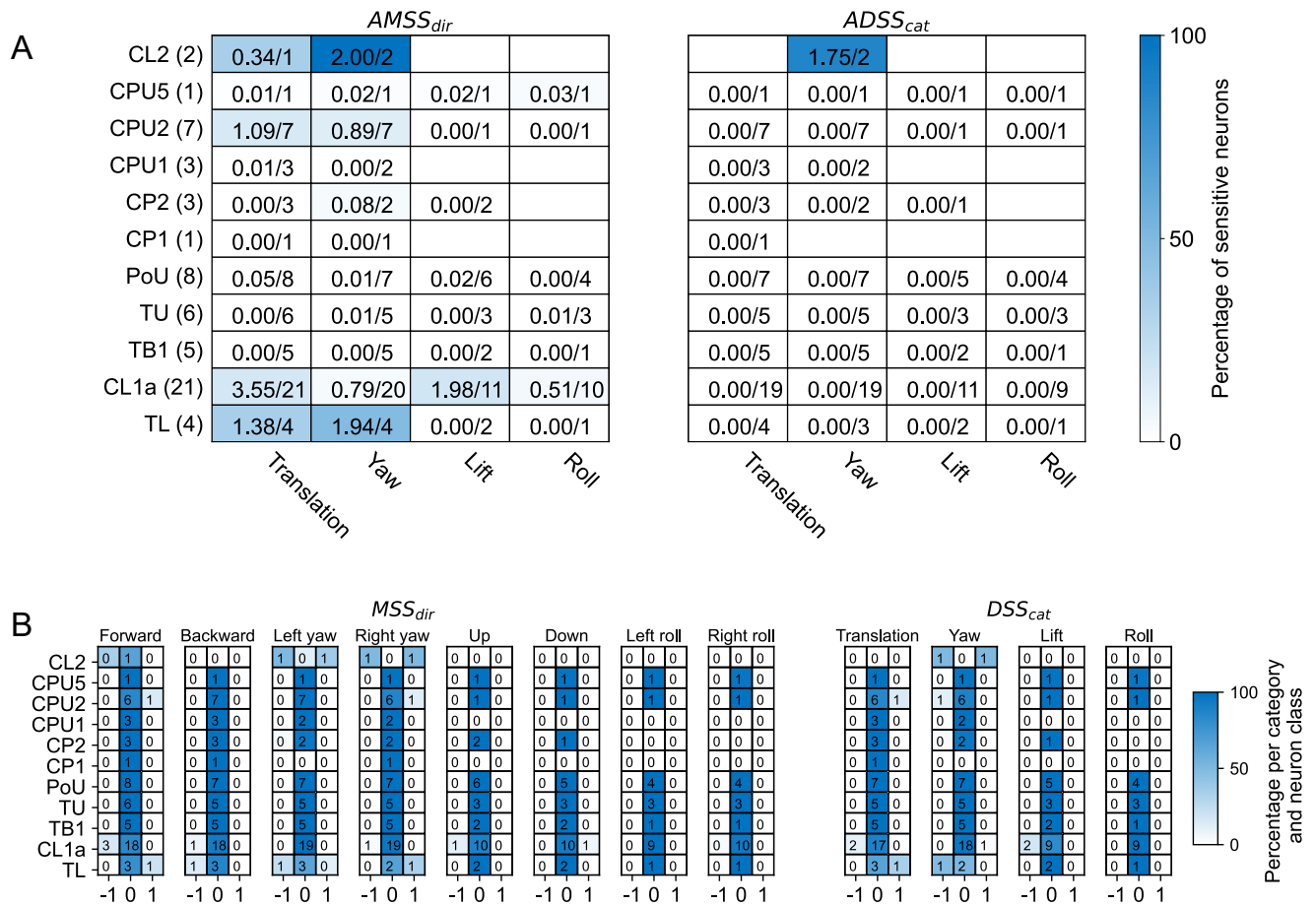


**Figure 3.** Overview of motion sensitivity and direction selectivity of all recorded neurons. **(A)** Absolute motion sensitivity scores per motion direction ( $AMSS_{dir}$ , left) and absolute direction selectivity scores per motion direction category ( $ADSS_{cat}$ , right), summed over neuron cell types. Absolute motion sensitivity scores take values between 0 and 1, with values close to 0 indicating no motion sensitivity and values close to 1 indicating motion selectivity, disregarding whether the neuron responds with an increase or decrease in activity. Absolute direction selectivity scores take values between 0 and 1, with values close to 0 indicating no direction selectivity and values close to 1 indicating direction selectivity, disregarding which motion direction elicits greater firing rates. Each cell holds the (rounded) sum of response scores over neuron cell types. Numbers are given as sums of scores over the total number of tested neurons. The fractions of summed scores and total possible scores are also indicated by the background color. The total number of recorded neurons for each neuron class is indicated in parentheses. Empty cells mean that no neuron was tested with the respective stimulus. **(B)** Distribution of motion sensitivity scores per motion direction ( $MSS_{dir}$ , left) and direction selectivity scores per direction category ( $DSS_{cat}$ , right), both per neuron class. Cell shading codes for the fraction of summed scores and total possible scores.

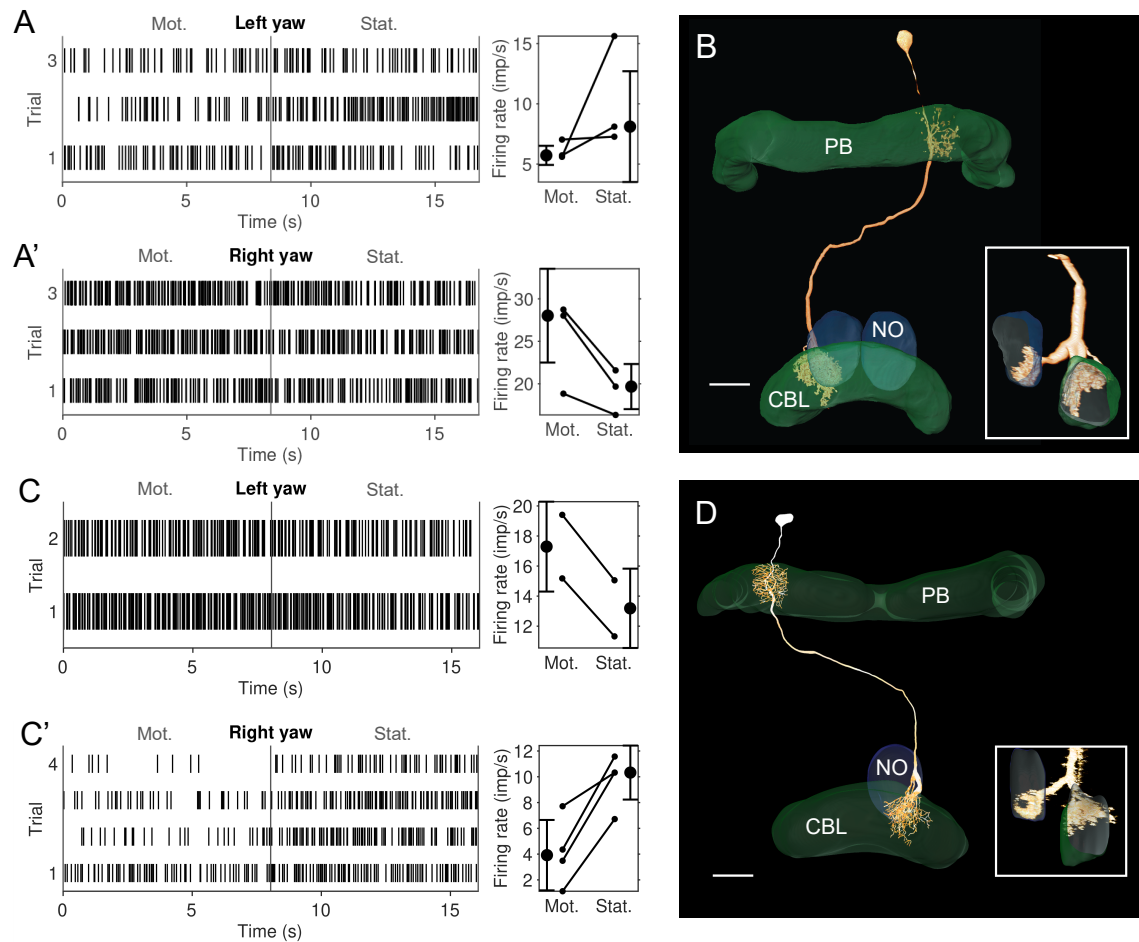


**Figure 4.** Physiological responses to yaw rotation and projections of CL2 neurons. **(A,A')** Physiological response (raster plots and mean firing rates) to left yaw rotation **(A)** and right yaw rotation **(A')** of the CL2 neuron shown in **B** (unit 801<sup>R</sup> in Supplementary Figures 1 and 2). The neuron shows reduced firing rate during simulated left yaw and increased firing activity during simulated right yaw. Vertical lines in the raster plots indicate onset of the stationary phase. **(B)** Skeleton view of the CL2 neuron (view from posterior) recorded in **A** and **A'**. The neurons arborized in column R4 of the right hemisphere of the protocerebral bridge (PB), layers 1-3 of column L2 in the CBL, and in the lower unit of the left NO. Inset shows sagittal view of ramifications in the lower division of the central body (CBL), and the left nodulus (NO). Scale bar: 40 μm. **(C,C')** Raster plots and changes in firing rate during simulated yaw in the second CL2 neuron, shown in **D** (unit 800<sup>L</sup> in Supplementary Figures 1 and 2). The neuron increased its firing rate during simulated left yaw **(C)** and decreased its firing rate during simulated right yaw **(C')**. **(D)** Two-dimensional reconstruction of the neuron from confocal image stacks (view from posterior). It arborized in column L4 of the left hemisphere of the PB, column R2 in the CBL, and in the lower unit of the right NO. Inset shows sagittal view illustrating ramifications in the CBL and NO. Scale bar: 40 μm.

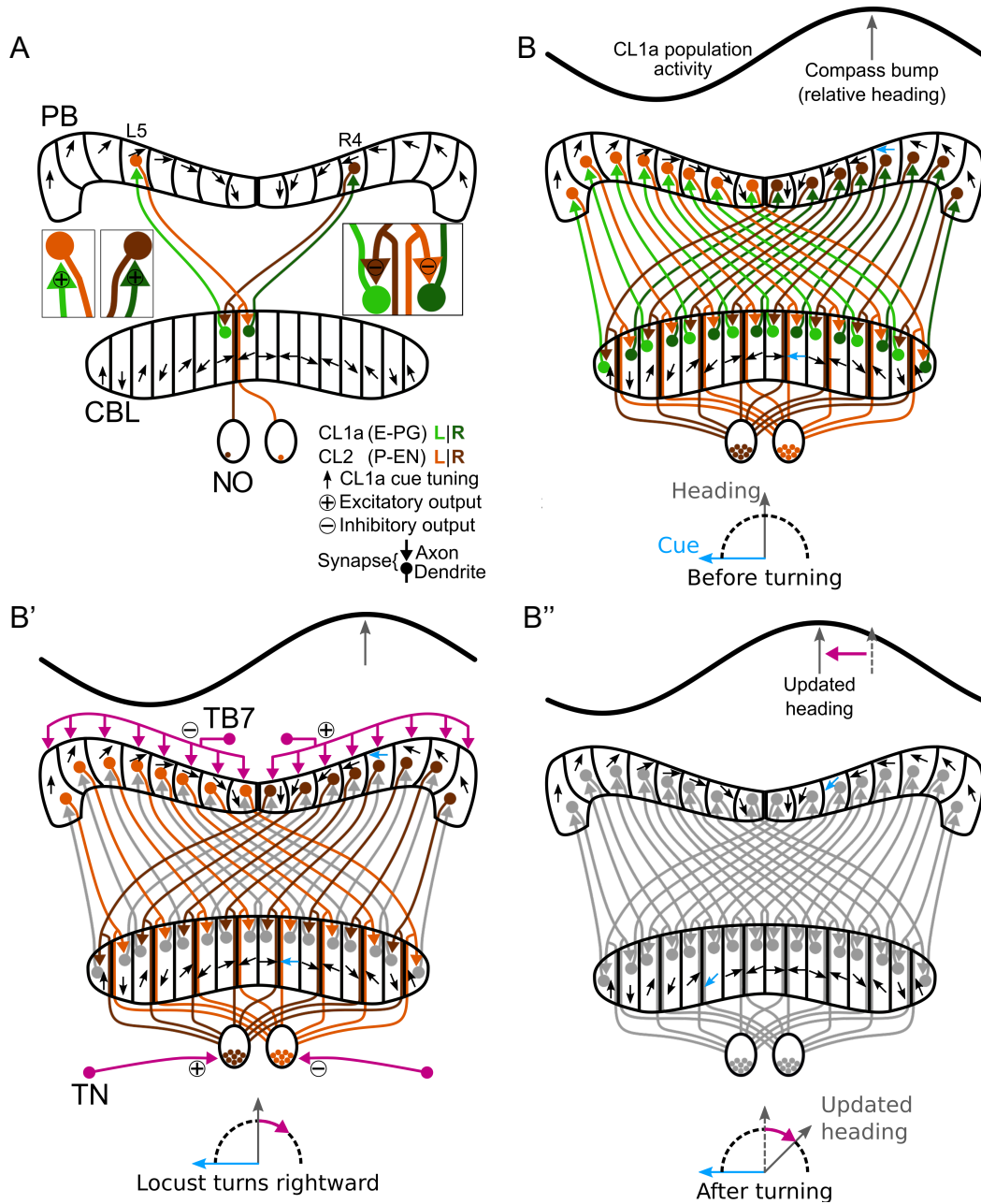


**Figure 5.** Schematic wiring diagram of CL1a and CL2 columnar neurons in the central complex and hypothetical shift mechanism of the internal heading signal in the PB. **(A)** Schematic wiring diagram of the CX with a subset of the involved neuron types: CL1a and CL2 neurons are connected to one another in the protocerebral bridge (PB) and lower division of the central body (CBL), while CL2 neurons also have postsynaptic arborizations in the noduli (NO). CL1a neurons are topographically tuned to solar azimuth along the PB (black arrows). **(B-B'')** Hypothetical shift mechanism of the internal heading signal in the PB. **(B)** Full population of CL1a and CL2 neurons and initial activity state in the network: With an environmental cue (sun) 90° left of the locust (bottom), the CL1a population activity (top) has a distinct maximum according to the neural tuning (highlighted arrows in PB and CBL). **(B')** When the locust turns right, CL2 neurons are excited or inhibited depending on their brain side. Neurons that innervate the left (right) NO are excited (inhibited) by tangential neurons (TN) from the lateral complexes and relay onto CL1a neurons from the left (right) half of the PB. This asymmetric input may analogously be conveyed in the PB by tangential neurons (TB7) from the superior posterior slope. **(B'')** After turning, the CL1a population activity maximum is shifted so that the neural heading estimate accordingly represents the new heading relative to the external cue. Wiring schemes from (Heinze and Homberg, 2008), topographic tuning in the PB and CBL based on (Zittrell et al., 2020).

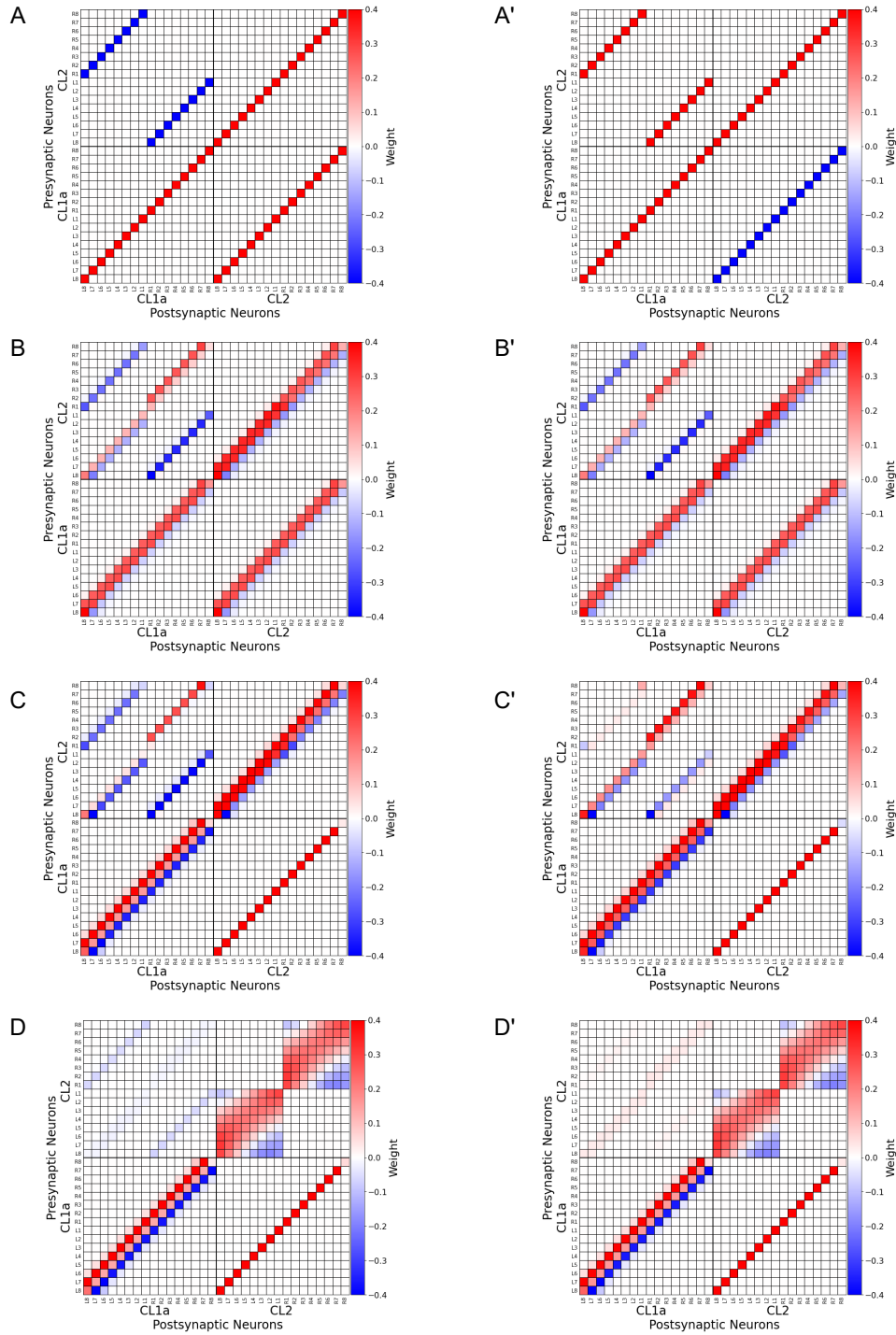


**Figure 6.** Computational Model. (A-A') Connectivity matrices representing the projection and connectivity schemes shown in Figure 5B, with additional self-recurrent excitatory connections. Excitatory synapses are depicted in red, inhibitory synapses in blue. Neurons are indexed via the PB column (L8-R8) in which they arborize. (A)  $M_A$ , implying excitatory synapses from CL1a onto CL2 neurons in the PB and inhibitory synapses from CL2 onto CL1a neurons in the CBL. (A')  $M_B$  implying a reversed polarity. (B-B') Relaxed versions  $M_{A_r}$  and  $M_{B_r}$  of the matrices shown in A-A' optimized to produce shifts of the activity patterns  $x$ . (C-C') Constrained versions  $M_{A_r,c}$  and  $M_{B_r,c}$  of  $M_{A_r}$  and  $M_{B_r}$ , representing broader arborizations in the CBL but not the PB (compared to  $M_A$  and  $M_B$ ). (D-D')  $M_{A_r,c,NO}$  and  $M_{B_r,c,NO}$ ; Same as C-C' but with added connections among CL2 neurons branching in the same hemisphere of the PB and the same nodule and optimized to shift activity patterns  $x$ .

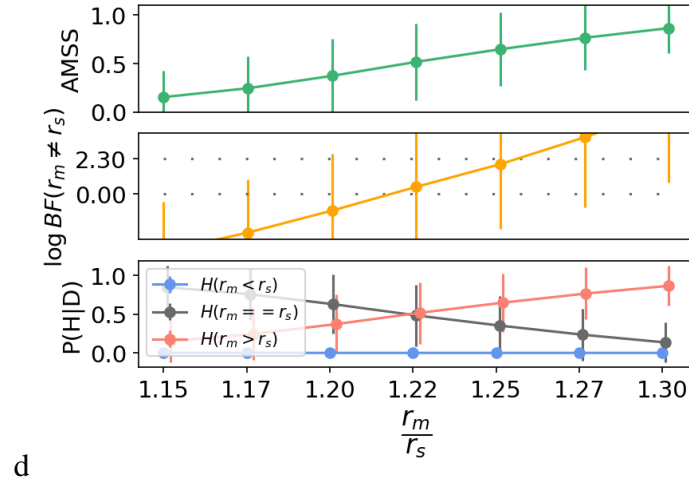


**Figure 7.** Power analysis of the Bayesian hypothesis comparison used for motion sensitivity analysis. The circles and error bars are means and standard deviations computed across 10,000 repetitions of a simulated experiment. The ratio of the motion phase firing rate  $r_m$  and  $r_s$  is shown along the abscissa. **Top:** absolute motion sensitivity (AMSS), cf. Equation 2. **Middle:** Bayes factor in favor of the hypothesis that the firing probabilities/rates are different during motion vs. equal rates, larger values represent stronger evidence. The dotted lines show the boundaries for weak and strong evidence according to Kass and Raftery (1995). **Bottom:** hypothesis posterior, used for the averaging of the motion sensitivity score (MSS), cf. Equation 1. The certainty of  $H(r_m > r_s)$  increases with an increasing  $\frac{r_m}{r_s}$  ratio.  $\frac{r_m}{r_s} \approx 1.25$  is sufficient for strong evidence on average. For details, see text.